

**LOCALIZATION OF MOVING SOURCES:
UNIQUENESS, STABILITY, AND BAYESIAN INFERENCE**

SÁRA WANG, MIRZA KARAMEHMEDOVIĆ, AND FAOUZI TRIKI

ABSTRACT. We consider the subsonic moving point source problem for the scalar wave equation in \mathbf{R}^3 , proving a regularity result for the direct problem, and uniqueness and stability results for the inverse problem. We then present and investigate numerically a Bayesian framework for the inference of the source trajectory and intensity from wave field measurements. The framework employs Gaussian process priors, the pre-conditioned Crank-Nicholson scheme with Markov Chain Monte Carlo sampling, and conditioning on functionals to include prior information on the source trajectory.

1. INTRODUCTION

This work concerns the moving source problem for the scalar wave equation in \mathbf{R}^3 ,

$$(1) \quad \begin{cases} c^{-2}\partial_t^2 u - \Delta u &= q(t)\delta_{p(t)} \in C^m([0, T[, \mathcal{E}'^0(\mathbf{R}^3)), \\ u(0+, x) &= 0, \quad x \in \mathbf{R}^3, \\ \partial_t u(0+, x) &= 0, \quad x \in \mathbf{R}^3. \end{cases}$$

Here $m \in \mathbf{N}$ is fixed, $c \in \mathbf{R}_+$ is the constant wave speed, $T \in \mathbf{R}_+$ is a fixed final time, $p \in C^{m+1}([0, T[, \Omega_0)$ is the source trajectory (with $\Omega_0 \subset \mathbf{R}^3$ an open, bounded, simply connected domain), $q \in C^m([0, T[)$ is the nonnegative-valued source intensity, δ_a is the Dirac delta supported at $a \in \mathbf{R}^3$, and $\mathcal{E}'^0(\mathbf{R}^3)$ is the space of compactly supported distributions. We consider subsonic sources, that is, we assume

$$(2) \quad |p'(t)| < c, \quad t \in]0, T[.$$

The fundamental solution $E_+ \in C^\infty([0, T[, \mathcal{E}'^0(\mathbf{R}^3))$ of the wave operator, given by [11, Section 6.2, Eqs. (6.2.4)' and (6.2.6)']

$$E_+(t)(\phi) = \frac{c^2 t}{4\pi} \int_{\omega \in S^2} \phi(ct\omega) d\omega, \quad t \in]0, T[, \quad \phi \in C^\infty(\mathbf{R}^3),$$

Date: April 12, 2022.

Department of Applied Mathematics and Computer Science, Technical University of Denmark, Denmark. Email: s144275@student.dtu.dk.

Department of Applied Mathematics and Computer Science, Technical University of Denmark, Denmark. Email: mika@dtu.dk. M. K. was supported by The Villum Foundation (grant no. 25893).

Laboratoire Jean Kuntzmann, UMR CNRS 5224, Université Grenoble-Alpes, 700 Avenue Centrale, 38401 Saint-Martin-d'Hères, France. E-mail: faouzi.triki@univ-grenoble-alpes.fr. F. T. was supported by the grant ANR-17-CE40-0029 of the French National Research Agency ANR (project MultiOnde).

satisfies

$$\begin{cases} (c^{-2}\partial_t^2 - \Delta)E_+(t) &= \delta_0, & t \in]0, T[, \\ E_+(0+) &= 0, \\ \partial_t E_+(0+) &= c^2\delta_0, \end{cases}$$

and the solution [11, Theorem 6.2.4]

$$\begin{aligned} u(t, \cdot) &= \int_0^t E_+(t-s) * (q(s)\delta_{p(s)}) ds \\ (3) \quad &= \frac{c^2}{4\pi} \int_0^t q(s)(t-s) \int_{\omega \in S^2} \delta_{c(t-s)\omega+p(s)} d\omega ds \in C^\infty(]0, T[, \mathcal{E}'^0(\mathbf{R}^3)), \end{aligned}$$

of (1) is the field radiated by the point source. It is well-known [14] that $u(t, x)$ can be expressed using the Liénard-Wiechert retarded potential

$$(4) \quad u(t, x) = \begin{cases} (c/4\pi)q(\tau(x, t))|x - p(\tau(x, t))|^{-1}h(x, \tau(x, t))^{-1}, & |x - p(0)| < ct, \\ 0 & \text{otherwise,} \end{cases}$$

where $\tau(x, t)$ is given implicitly by

$$(5) \quad c(t - \tau(x, t)) = |x - p(\tau(x, t))|,$$

and

$$(6) \quad h(x, \tau) = c - \frac{x - p(\tau)}{|x - p(\tau)|} p'(\tau) \quad \text{for } x \neq p(\tau).$$

Notice that since p satisfies the inequality (2), we have

$$\frac{d}{d\tau} (\tau \mapsto t - c^{-1}|x - p(\tau)|) \leq c^{-1}|p'(\tau)| < 1,$$

so the fixed point problem (5) has a unique solution.

Now let Ω be a bounded and connected domain with a C^2 boundary $\partial\Omega$, and such that $\bar{\Omega}_0 \subset \Omega$. We denote by $\nu(x)$ the unit outward normal vector at $x \in \partial\Omega$. In the following we measure the trace of the solution u at the *measurement surface* $\Gamma \subseteq \partial\Omega$ that is open in the induced topology on $\partial\Omega$, and that is not included in any plane intersecting Ω . The inverse moving source problem we consider is to reconstruct p and q , given a measurement $u|_{[0, T] \times \Gamma}$; the associated forward problem is to find u given p and q . We must *turn off* the source at a time $T_0 < T$ (i.e., $q(t) = 0$ for $t \in [T_0, T]$) to have any chance of uniqueness of solution of the inverse problem, due to the finite speed of wave propagation. We consider T large enough to allow the information about p and q for $t \in [0, T_0]$ to propagate towards the measurement set Γ , that is,

$$(7) \quad T > T_0 + \sup\{|x - y|/c, x \in \Gamma, y \in \Omega_0\} := T^*.$$

We further assume that the set $\{t \in [0, T_0], q(t) = 0\}$ has zero measure. This prevents the situation where two trajectories are indistinguishable because the source does not radiate where the trajectories are not aligned. Finally, if Γ is included in a plane P intersecting Ω then one is unable to distinguish the field measurements from pairs of sources constructed using the same intensity, and by translating a trajectory confined in $P \cap \Omega$ to two different planes parallel to P and at the same orthogonal distance from P . (More generally, trajectories mirrored across P and having the same amplitude profile q would also produce the same field measurements.)

The inverse moving source problem for the wave equation was treated in many recent works [20, 17, 13, 12, 10]. Different approaches have been considered for solving it. In [8, 21], the authors have applied direct algebraic methods for reconstructing stationary point sources from boundary measurement. Later, in [20], this approach was extended to the problem of moving sources with a strong assumption on their trajectories. A different algebraic method for the identification of a single moving source using measurements of the retarded potential and all its derivatives at a single observation point was provided in [18]. Optimization techniques were also applied in solving the inverse problem (see for instance [5, 15, 16, 22]). Recently a Lipschitz stability estimate was derived for recovering a single moving point source from the knowledge of the field at six well-chosen points on the boundary assuming that the intensity is a known constant [10]. Notice that when the point source is stationary the inverse problem is well studied, and Hölder type stability estimates are derived using a single boundary measurement [2, 3].

Our main theoretical results concern the regularity of solution of the forward problem, and the uniqueness and stability of solution of the inverse problem.

Theorem 1. *Let u be the solution of the system (1). Then*

$$u \in C^\infty(]0, T[, H^{m-1/2-\varepsilon}(\mathbf{R}^3)),$$

for every strictly positive ε . Moreover,

$$u \in C^\infty(]0, T[, C^\infty(\mathbf{R}^3 \setminus \cup_{s=0}^{T_0} \overline{B_{p(s)}(c(T_0 - s))})),$$

and $u(t, \cdot)$ is C^∞ in

$$\left\{ |x - p(s)| < c(t - s), 0 \leq s \leq \min\{t, T_0\} \right\} \setminus p([0, T_0]).$$

Finally,

$$u(t, \cdot)|_\Gamma = 0 \quad \text{for } t \in]T^*, +\infty[,$$

with $T^* = T_0 + \sup\{|x - y|/c, x \in \Gamma, y \in \Omega_0\}$.

Theorem 2. *Assume that $\partial\Omega$ is real analytic. Then the field measurement $u|_{[0, T] \times \Gamma}$ determines the source trajectory p and intensity q uniquely.*

Theorem 3. *Let u_j be the solution of the system (1) with $q = q_j$, and $p = p_j$ for $j = 1, 2$. Assume that $\|q_j\|_{C^1([0, T_0])} \leq M_q$ and $\|p_j\|_{C^2([0, T_0])} \leq M_p$ for $j = 1, 2$.*

Let $\rho \in]0, T_0[, q_0$ and c_0 be strictly positive constants. Assume

$$(8) \quad q_j(t) \geq q_0, \quad \forall t \in [0, T_0 - \rho],$$

and

$$(9) \quad 1 - c^{-1}p'_j(t) \geq c_0, \quad \forall t \in [0, T], j = 1, 2.$$

Let

$$\varepsilon = \sup_{\widehat{k} \in S^2} \int_{\mathbf{R} \times \partial\Omega} \left(c^{-1} |\partial_t u(t - c^{-1}\widehat{k} \cdot x, x)| + |\partial_\nu u(t - c^{-1}\widehat{k} \cdot x, x)| \right) H(t - c^{-1}\widehat{k} \cdot x) d\sigma(x) dt,$$

where $u = u_1 - u_2$. Then for $\varepsilon \in]0, q_0(T_0 - \rho)[$, we have

$$(10) \quad \|q_1 - q_2\|_{C^0([0, T_0 - \rho])} + \|p_1 - p_2\|_{C^0([0, T_0 - \rho])} \leq C\varepsilon,$$

where H is the Heaviside function, and $C > 0$ is a constant that only depends on $c_0, q_0, T_0, c, M_q,$ and M_p .

We prove Theorems 1–3 in Section 2, and describe our framework for Bayesian inference of source amplitudes and trajectories in Section 3. Finally, we show and discuss our numerical results in Section 4.

2. PROOFS OF THEOREMS 1–3

2.1. Proof of Theorem 1 (regularity of solution of the forward problem).

Using the fact that

$$\begin{aligned} \int_{\omega \in S^2} \exp\left(-ic(t-s)|\xi| \frac{\xi}{|\xi|} \cdot \omega\right) d\omega &= \int_0^\pi \int_0^{2\pi} \exp(-i|\xi|c(t-s)\cos\theta) \sin\theta d\varphi d\theta \\ &= \frac{4\pi}{c(t-s)} \frac{\sin(|\xi|c(t-s))}{|\xi|}, \end{aligned}$$

we get

$$\begin{aligned} \widehat{u}(t, \xi) &= \frac{c^2}{4\pi} \int_0^t (t-s)q(s) \int_{\omega \in S^2} (\delta_{c(t-s)\omega+p(s)})_x (e^{-ix\xi}) d\omega ds \\ (11) \quad &= \frac{c}{|\xi|} \int_0^t q(s) \sin(c|\xi|(t-s)) e^{-i\xi p(s)} ds, \end{aligned}$$

Since $u(t, \cdot) \in \mathcal{E}^0(\mathbf{R}^3)$, we know by the Paley-Wiener-Schwartz theorem [11, Theorem 7.3.1] that $\widehat{u}(t, \cdot)$ is entire in \mathbf{C}^3 and that $|\widehat{u}(t, \cdot)|$ is bounded in \mathbf{R}^3 by a constant \widetilde{C} ; in particular, the singularity at zero in (11) is removable, and for every $\xi \in \mathbf{R}^3$, $t \in [0, T]$, we have

$$\begin{aligned} 2c^{-1}|\xi||\widehat{u}(t, \xi)| &\leq \left| \int_0^t q(s) \exp(i|\xi|f_+(s, t, \xi/|\xi|)) ds \right| \\ &\quad + \left| \int_0^t q(s) \exp(i|\xi|f_-(s, t, \xi/|\xi|)) ds \right|, \end{aligned}$$

where $f_\pm(s, t, \omega) = \pm c(t-s) - p(s) \cdot \omega$ for $s \in [0, T]$, $t \in [0, T]$, and $\omega \in S^2$. The real-valued functions $\partial_s f_\pm(s, t, \omega) = \mp c - p'(s) \cdot \omega$ are nonzero for all s, t , and ω , so we can use integration by parts to write

$$\begin{aligned} \left| \int_0^t q(s) e^{i|\xi|f_\pm(s, t, \xi/|\xi|)} ds \right| &= \left| \int_0^t q(s) \left(\frac{1}{i|\xi|\partial_s f_\pm(s, t, \xi/|\xi|)} \frac{\partial}{\partial s} \right)^m e^{i|\xi|f_\pm(s, t, \xi/|\xi|)} ds \right| \\ &= |\xi|^{-m} \left| W(t, \xi/|\xi|) + \int_0^t Q(s, t, \xi/|\xi|) e^{i|\xi|f_\pm(s, t, \xi/|\xi|)} ds \right| \\ &\leq |\xi|^{-m} \left(|W(t, \xi/|\xi|)| + \int_0^t |Q(s, t, \xi/|\xi|)| ds \right), \end{aligned}$$

for some functions W and Q continuous w.r.t. all their arguments because $q \in C^m$ and $p \in C^{m+1}$, and because all s -derivatives of f_\pm are continuous w.r.t. t and ω . But the sets $[0, T]$ and S^2 are compact, so there is a finite constant C , independent of t and of $\xi/|\xi|$, satisfying $|\widehat{u}(t, \xi)| \leq C|\xi|^{-m-1}$ for all $t \in [0, T]$, $\xi \in S^2$. Thus, for

$\sigma < m - 1/2$,

$$\begin{aligned} \|(1 + |\xi|^2)^{\sigma/2} \widehat{u}(t, \cdot)\|_{L^2(\mathbf{R}^3)}^2 &\leq 2^\sigma 4\pi \widetilde{C}^2/3 + 4\pi C^2 \int_{r=1}^{\infty} r^{-2m} (1 + r^2)^\sigma dr \\ &\leq 2^{\sigma+2} \pi \left(\widetilde{C}^2/3 + C^2 \left[\frac{r^{2(\sigma-m)+1}}{2(\sigma-m)+1} \right]_{r=1}^{\infty} \right) < \infty. \end{aligned}$$

To prove the second part of the theorem, we use the fact that [7, p. 130]

$$\begin{aligned} \text{sing supp } E_+(t-s) * (q(s)\delta_{p(s)}) &\subset \text{sing supp } E_+(t-s) + \text{sing supp } q(s)\delta_{p(s)} \\ &= \{y+z, |y|=c(t-s), z=p(s)\} \end{aligned}$$

for $t \in [0, T]$ and $s \in [0, T_0]$. Specifically,

$$\text{sing supp } u(t, \cdot) \subset \bigcup_{s=0}^{\min\{t, T_0\}} \{y+z, |y|=c(t-s), z=p(s)\}, \quad t \in [0, T],$$

and finally

$$\begin{aligned} \bigcup_{t=0}^T \text{sing supp } u(t, \cdot) &\subset \bigcup_{t=0}^{T_0} \bigcup_{s=0}^{\min\{t, T_0\}} \{y+z, |y|=c(t-s), z=p(s)\} \\ &= \bigcup_{s=0}^{T_0} \overline{B_{p(s)}(c(T_0-s))}. \end{aligned}$$

This completes the regularity result of the theorem. Finally, we deduce from (5) that $\tau(t, x)$ satisfies

$$(12) \quad t - \sup\{|x-y|/c, x \in \Gamma, y \in \Omega_0\} \leq \tau(x, t) \leq t \quad \text{for all } t > 0, x \in \Gamma.$$

Since $q(t)$ is supported in $[0, T_0]$, we obtain that $u(t, \cdot)|_{\Gamma}$ is also supported in $[0, T^*]$, which finishes the proof of Theorem 1.

2.2. Proof of Theorem 2 (uniqueness of solution of the inverse problem).

Under the assumptions in Section 1, the partial Fourier transform of $q(t)\delta_{p(t)}$ w.r.t. t is well-defined in $\mathcal{E}'^0(\mathbf{R}^3)$, with support in $p([0, T_0])$. Indeed, for any $\phi \in C_0^\infty(\mathbf{R}^3)$ and any real ω , we have

$$\begin{aligned} \left| \left(\int_{t \in \mathbf{R}_+} e^{-i\omega t} q(t) \delta_{p(t)} dt \right) (\phi) \right| &= \left| \int_{t=0}^{T_0} e^{-i\omega t} q(t) \phi(p(t)) dt \right| \\ &\leq T_0 \|q\|_{L^\infty([0, T_0])} \|\phi\|_{L^\infty(p([0, T_0]) \cap \text{supp } \phi)}. \end{aligned}$$

Now assume u_1 and u_2 satisfy (1) with sources $q_1(t)\delta_{p_1(t)}$ and $q_2(t)\delta_{p_2(t)}$, respectively, and such that $u_1|_{[0, T] \times \Gamma} \equiv u_2|_{[0, T] \times \Gamma}$. Writing $u = u_1 - u_2$ and $f(t, \cdot) = q_1(t)\delta_{p_1(t)} - q_2(t)\delta_{p_2(t)}$, we have

$$(13) \quad \begin{cases} c^{-2} \partial_t^2 u - \Delta u &= f(t, \cdot) \quad \text{in } C_0(\mathbf{R}, \mathcal{E}'^0(\mathbf{R}^3)), \\ u(x, 0) &= 0, \quad x \in \mathbf{R}^3, \\ \partial_t u(x, 0) &= 0, \quad x \in \mathbf{R}^3, \\ u|_{\Gamma \times \mathbf{R}} &\equiv 0. \end{cases}$$

The last equation in (13) follows from (4) and the fact that u is supported in $[0, T]$. Taking the partial Fourier transform of the wave equation in (13) with respect to t , we get $(\Delta + (\omega/c)^2) \widehat{u}(\omega, x) = -\widehat{f}(\omega, x)$, so, since $\text{supp } \widehat{f}(\omega, \cdot) \cap \partial\Omega = \emptyset$, we have $(\Delta + (\omega/c)^2) \widehat{u}(\omega, x) = 0$ for x in a nonempty open neighborhood N of $\partial\Omega$.

The ellipticity of the Helmholtz operator $\Delta + (\omega/c)^2$ now implies that $\widehat{u}(\omega, x)$ is real-analytic w.r.t. x in N . We have furthermore that $\widehat{u}(\omega, x) \equiv 0$ for $x \in \Gamma$. If Γ is boundaryless then $\Gamma = \partial\Omega$. Assuming $\partial\Gamma \neq \emptyset$, pick $x \in \partial\Gamma$. There is an open neighborhood $N_x \subseteq N$ of x and a biholomorphism ϕ mapping N_x to an open neighborhood of the origin in \mathbf{R}^3 , such that $\phi(x) = 0$, $\phi(N_x \cap \Omega) \subset \mathbf{R}^2 \times \mathbf{R}_-$, $\phi(N_x \cap \mathbb{C}\Omega) \subset \mathbf{R}^2 \times \mathbf{R}_+$, and $\phi(N_x \cap \partial\Omega) \subset \mathbf{R}^2 \times \{0\}$. The function $\widehat{U}(\omega, x') = \widehat{u}(\omega, \phi^{-1}(x', 0))$ is real analytic in $\phi(N_x \cap \partial\Omega)$, and $\widehat{U} \equiv 0$ in $\phi(N_x \cap \Gamma)$, which implies $\widehat{U} \equiv 0$ in $\phi(N_x \cap \partial\Omega)$ by the identity theorem for holomorphic functions, as $\phi(N_x \cap \Gamma)$ is a nonempty open subset of $\phi(N_x \cap \partial\Omega)$. Since $\partial\Omega$ can be covered by a finite number of biholomorphic local charts, we conclude that $\widehat{u}(\omega, \cdot) \equiv 0$ at $\partial\Omega$. Thus, for any choice of open $\Gamma \subseteq \partial\Omega$, the function $\widehat{u}(\omega, \cdot)$ satisfies the exterior Helmholtz problem

$$(14) \quad \begin{cases} (\Delta + (\omega/c)^2)\widehat{u}(\omega, x) = 0, & x \in \mathbf{R}^3 \setminus \overline{\Omega}, \\ \widehat{u}(\omega, x) = 0, & x \in \partial\Omega, \\ \lim_{|x| \rightarrow \infty} |x|(\partial_{|x|}\widehat{u} - i(\omega/c)\widehat{u}) = 0, & \text{uniformly in } x/|x| \in S^2. \end{cases}$$

The Sommerfeld radiation condition in \mathbf{R}^3 , which is the last equation in (14), is satisfied by \widehat{u} because the support of the source $\widehat{f}(\omega, \cdot)$ has a compact support; indeed, $\widehat{f}(\omega, x) = 0$ if $x \notin p_1([0, T_0]) \cup p_2([0, T_0])$. But (14) is known [19, Theorem 2.6.5, p. 102] to have only the trivial solution. In particular $\widehat{u} = \partial_\nu \widehat{u} = 0$ at $\partial\Omega$, and hence \widehat{u} solves the interior Helmholtz problem

$$(15) \quad \begin{cases} (\Delta + (\omega/c)^2)\widehat{u}(\omega, x) = -\widehat{f}(\omega, x), & \text{in } \Omega, \\ \widehat{u}(\omega, x) = 0, & x \in \partial\Omega, \\ \partial_\nu \widehat{u}(\omega, x) = 0, & x \in \partial\Omega. \end{cases}$$

Since $\widehat{f}(\omega, \cdot)$ has a compact support $p_1([0, T_0]) \cup p_2([0, T_0])$, which has a zero two-dimensional Hausdorff measure, we deduce from the uniqueness of Cauchy problem, $\widehat{u} = 0$ a. e. in Ω . On the other hand a simple calculation shows that $\widehat{f}(\omega, \cdot) \in W^{-1,p}(\mathbf{R}^3)$ for all $p \in [1, \frac{3}{2}[$, which regarding to the elliptic regularity implies that $\widehat{u}(\omega, \cdot) \in W_{loc}^{1,p}(\mathbf{R}^3)$ for all $p \in [1, \frac{3}{2}[$. Consequently $\widehat{u} = 0$ in $\mathcal{E}'^0(\mathbf{R}^3)$. We then obtain $\widehat{f}(\omega, \cdot) = 0$, which completes the proof of Theorem 2.

2.3. Proof of Theorem 3 (stability of solution of the inverse problem).

Let u_1 and u_2 satisfy (1) with sources $q_1(t)\delta_{p_1(t)}$ and $q_2(t)\delta_{p_2(t)}$, respectively, and such that $u_1 - u_2$ and $\partial_\nu(u_1 - u_2)$ are given on $[0, T] \times \partial\Omega$. Writing $u = u_1 - u_2$ and $f(t, \cdot) = q_1(t)\delta_{p_1(t)} - q_2(t)\delta_{p_2(t)}$, we have

$$(16) \quad \begin{cases} c^{-2}\partial_t^2 u - \Delta u = f(t, \cdot) & \text{in } C_0(\mathbf{R}, \mathcal{E}'^0(\mathbf{R}^3)), \\ u(x, 0) = 0, & x \in \mathbf{R}^3, \\ \partial_t u(x, 0) = 0, & x \in \mathbf{R}^3, \end{cases}$$

Applying the partial Fourier transform to the wave equation in (16) with respect to t , we obtain

$$(17) \quad \begin{cases} (\Delta + (\omega/c)^2)\widehat{u}(\omega, x) = -\widehat{f}(\omega, x), & x \in \mathbf{R}^3, \\ \lim_{|x| \rightarrow \infty} |x|(\partial_{|x|}\widehat{u} - i(\omega/c)\widehat{u}) = 0 & \text{uniformly in } x/|x| \in S^2. \end{cases}$$

Let $\widehat{k} \in S^2$ be fixed. Multiplying the Helmholtz equation by $e^{-i\frac{\omega}{c}\widehat{k}\cdot x}$, and integrating by parts yield

$$\begin{aligned} \int_{t \in \mathbf{R}_+} q_1(t) e^{-i(\omega/c)\widehat{k}\cdot p_1(t)} e^{-i\omega t} dt - \int_{t \in \mathbf{R}_+} q_2(t) e^{-i(\omega/c)\widehat{k}\cdot p_2(t)} e^{-i\omega t} dt \\ = - \int_{\partial\Omega} \left(i\frac{\omega}{c}\widehat{k} \cdot \nu \widehat{u} + \partial_\nu \widehat{u} \right) e^{-i\frac{\omega}{c}\widehat{k}\cdot x} d\sigma(x). \end{aligned}$$

Making the change of variables $t = \varphi_j(\tau)$ where $\tau = \varphi_j(\tau) + c^{-1}\widehat{k}\cdot p_j(\varphi_j(\tau))$, $j = 1, 2$, respectively in the two integrals on the left side give

$$(18) \quad \int_{\tau \in \mathbf{R}} \left(\frac{\chi_1(\tau) q_1(\varphi_1(\tau))}{c^{-1}\widehat{k}\cdot p'_1(\varphi_1(\tau)) + 1} - \frac{\chi_2(\tau) q_2(\varphi_2(\tau))}{c^{-1}\widehat{k}\cdot p'_2(\varphi_2(\tau)) + 1} \right) e^{-i\omega\tau} d\tau = \\ - \int_{\partial\Omega} \left(i\frac{\omega}{c}\widehat{k} \cdot \nu \widehat{u} + \partial_\nu \widehat{u} \right) e^{-i\frac{\omega}{c}\widehat{k}\cdot x} d\sigma(x),$$

where $\chi_j(\tau) = H(\tau - \tau_j)$, with $\tau_j = \varphi_j^{-1}(0) = c^{-1}\widehat{k}\cdot p_j(0)$, $j = 1, 2$, and H is the Heaviside function. Since $\varphi_j, j = 1, 2$, are strictly increasing functions, we also have $\chi_j(\tau) = H(\varphi_j(\tau)), j = 1, 2$.

Applying the Fourier transform inverse both sides, we get

$$(19) \quad \frac{\chi_1(\tau) q_1(\varphi_1(\tau))}{c^{-1}\widehat{k}\cdot p'_1(\varphi_1(\tau)) + 1} - \frac{\chi_2(\tau) q_2(\varphi_2(\tau))}{c^{-1}\widehat{k}\cdot p'_2(\varphi_2(\tau)) + 1} = \\ - \int_{\partial\Omega} \left(c^{-1}\widehat{k} \cdot \nu \partial_t u(\tau - c^{-1}\widehat{k} \cdot x, x) + \partial_\nu u(\tau - c^{-1}\widehat{k} \cdot x, x) \right) H(\tau - c^{-1}\widehat{k} \cdot x) d\sigma(x),$$

for all $\tau \in \mathbf{R}$.

Recall that Theorem 1 implies that $u \in C^\infty(]0, T[, H^{m-1-\varepsilon}(\partial\Omega))$, and hence the right hand side term is indeed well defined.

Notice that $\varphi_j(\tau), \tau_j, j = 1, 2$, as well as $\tau_j, j = 1, 2$, are also functions of \widehat{k} . Next our strategy is to first estimate $\|p_1(0) - p_2(0)\|$ in terms of the boundary measurements.

Without loss of generality one can assume that $\tau_1 \leq \tau_2$. Integrating (19) both sides over $] \tau_1, \tau_2[$, yields

$$(20) \quad \int_0^{\varphi_1(\tau_2)} q_1(s) ds = \int_{\tau_1}^{\tau_2} \frac{q_1(\varphi_1(t))}{c^{-1}\widehat{k}\cdot p'_1(\varphi_1(t)) + 1} dt \leq \varepsilon.$$

We claim that $\varphi_1(\tau_2) \in]0, T_0 - \rho[$. Indeed, assuming that $\varphi_1(\tau_2) > T_0 - \rho$, we deduce from (8), and (20), $q_0(T_0 - \rho) < \varepsilon$, which is in contradiction with the fact that $\varepsilon \in]0, q_0(T_0 - \rho)[$.

Therefore $\varphi_1(\tau_2) \in]0, T_0 - \rho[$, and hence

$$(21) \quad |\tau_2 - \tau_1| \leq 2q_0^{-1}\varepsilon.$$

Since the right hand side term is independent of \widehat{k} , we also get

$$(22) \quad \|p_1(0) - p_2(0)\| \leq 2cq_0^{-1}\varepsilon.$$

Let $\widehat{k}_0 = \widehat{k}(t_0) \in S^2$ such that $\widehat{k}_0 \cdot (p_1(t_0) - p_2(t_0)) = 0$. We deduce from (19) that

$$(23) \quad \left| \frac{q_1(t_0)}{\pm c^{-1}\widehat{k}_0 \cdot p'_1(t_0) + 1} - \frac{q_2(t_0)}{\pm c^{-1}\widehat{k}_0 \cdot p'_2(t_0) + 1} \right| \leq \varepsilon.$$

Simple calculations yield

$$|q_1(t_0) - q_2(t_0)| \leq 4\varepsilon.$$

Since t_0 is arbitrarily, we obtain

$$(24) \quad \|q_1 - q_2\|_{C^0([0, T_0])} \leq 4\varepsilon.$$

Integrating the identity (19) both sides over $] - \infty, r[$, with $r > 0$, gives

$$(25) \quad \left| \int_0^{\varphi_1(r)} q_1(s) ds - \int_0^{\varphi_2(r)} q_2(s) ds \right| \leq \varepsilon,$$

Combining (24) and (25) lead to

$$(26) \quad \left| \int_{\varphi_1(r)}^{\varphi_2(r)} q_2(s) ds \right| \leq (1 + 4T_0)\varepsilon,$$

for all $r \in]r_1, r_2[$ with

$$r_2 = \min_{j=1,2} \varphi_j^{-1}(T_0 - \rho), \quad r_1 = \max_{j=1,2} \varphi_j^{-1}(0) = \max_{j=1,2} \tau_j.$$

Notice that $r \in]r_1, r_2[$ is equivalent to $\varphi_j(r) \in]0, T_0 - \rho[$, $j = 1, 2$.

Using assumption (8), we find

$$(27) \quad |\varphi_2(r) - \varphi_1(r)| \leq q_0^{-1}(1 + 4T_0)\varepsilon,$$

for all $r \in]r_1, r_2[$.

Without loss of generality we further assume $r_2 = \varphi_1^{-1}(T_0 - \rho)$.

Further C designate a strictly positive constant that only depends on c_0 , q_0 , T_0 , c , M_q , and M_p .

Combining identities (19), (24), and (27), we obtain

$$|q_1(\varphi_1(r))| \left| \widehat{k} \cdot (p'_1(\varphi_1(r)) - p'_2(\varphi_1(r))) \right| \leq C\varepsilon, \quad \forall r \in]r_1, r_2[, \forall \widehat{k} \in S^2,$$

which in turn implies

$$(28) \quad \|p'_1(t) - p'_2(t)\|_{C^0([\varphi_1(r_1), T_0 - \rho])} \leq C\varepsilon.$$

We deduce from (21) the following inequality

$$(29) \quad |r_1 - \tau_1| \leq 2q_0^{-1}\varepsilon.$$

Using estimates (22), (28), and (29), we finally get

$$(30) \quad \|p_1(t) - p_2(t)\|_{C^0([0, T_0 - \rho])} \leq C\varepsilon,$$

which achieves the proof of the theorem.

3. BAYESIAN INFERENCE OF SOURCE TRAJECTORY AND INTENSITY

We next describe our setup for the Bayesian inference of the source trajectory and intensity. We confine the source trajectory $p(t)$ to the xy -plane, setting $p(t) = (p_x(t), p_y(t), 0)$, and impose GP (Gaussian process) priors on $p_x(t)$, $p_y(t)$, and $q(t)$. In our case, a GP is a stochastic process $g : \mathbf{R} \rightarrow \mathbf{R}$ such that for any $d \in \mathbf{N}$ and any $t_1, \dots, t_d \in [0, T_0]$ the distribution of the d -tuple $(g(t_1), \dots, g(t_d))$ is multivariate Gaussian. We write $g \sim \mathcal{GP}(m, k)$, where $m(t)$, $t \in [0, T_0]$, is the mean function and $k(t, t')$, $t, t' \in [0, T_0]$, is the covariance function. The mean and the covariance functions influence the dimensionality, smoothness, stationarity, periodicity, and other properties of the realizations of the GP. We choose the squared-exponential (SE) kernel

$$k_{\text{SE}}(t, t') = \kappa^2 \exp(-(t - t')^2 / 2\ell^2), \quad t, t' \in [0, T],$$

where the hyperparameters κ and ℓ are the magnitude and the correlation length, respectively. The magnitude controls the extent to which realizations of the GP can deviate from the mean, while the correlation length determines the speed with which these realizations can oscillate (larger ℓ gives slower oscillation). The SE kernel results in a smooth prior on the functions sampled from the GP, and corresponds to the use of radial basis functions ϕ_j . Also, $g \sim \mathcal{GP}(0, k_{\text{SE}})$ is second-order stationary, since k_{SE} is isotropic. We impose independent GP priors on the latent functions $p_x(t)$, $p_y(t)$ and $q(t)$: $p_x(t) \sim \mathcal{GP}(0, k_{\text{SE}}^p)$, $p_y(t) \sim \mathcal{GP}(0, k_{\text{SE}}^p)$, $q(t) \sim \mathcal{GP}(0, k_{\text{SE}}^q)$. The superscripts p and q indicate possibly separate choices of the hyperparameter values for the GP priors. Our measurement data $(X_i, U_i)_{i=1}^N$ consist of the field sampling times and sensor locations $X_i = (t_i, x_i, y_i, z_i)$ and sampled field values $U_i = u(t_i, x_i, y_i, z_i)$, where $N = N_s N_t$ is the product of the number N_s of sensors and the number N_t of samplings. We want to estimate $f = (p_x(t), p_y(t), q(t))$, having the forward mapping G from parameter space to data space given by

$$G(f)(X_i) = \begin{cases} \frac{c}{4\pi} \frac{q(\tau(X_i))}{|(x_i, y_i, z_i) - p(\tau(X_i))| h((x_i, y_i, z_i), \tau(X_i))}, & |(x_i, y_i, z_i) - p(0)| < ct_i, \\ 0 & \text{otherwise.} \end{cases}$$

The output is related to the input by $U_i = G(f)(X_i) + e$, with $e \sim \mathcal{N}(0, \beta^{-1}I)$ for some likelihood precision β . Thus, the field measurements are distributed according to

$$\mathbf{U} | p_x, p_y, q \sim \mathcal{N}(G(p_x, p_y, q)(\mathbf{X}), \beta^{-1} \mathbf{I}_{N \times N}),$$

and the Bayesian posterior for the latent functions is given by

$$\mathcal{P}(p_x, p_y, q | \mathbf{U}) = \frac{\mathcal{P}(\mathbf{U} | p_x, p_y, q) \mathcal{P}(p_x) \mathcal{P}(p_y) \mathcal{P}(q)}{\mathcal{P}(\mathbf{U})}.$$

The nonlinearity of G makes an analytic treatment of the posterior intractable, and we resort to a Markov Chain Monte Carlo (MCMC) numerical procedure. We evaluate the unknown functions at a set of sampling time points $\boldsymbol{\tau} \in [0, T_0]^M$. We let \vec{p}_x, \vec{p}_y and \vec{q} be the unknown functions and \vec{K} be the kernel evaluated at the grid $\boldsymbol{\tau}$. Note that the number of sampling points M , used to numerically sample

the latent functions, is not related to the number of measurement point N . The posterior density for the latent functions sampled on $\boldsymbol{\tau}$ is then

$$(31) \quad \mathcal{P}(\mathbf{f}|\mathbf{U}) = \frac{\mathcal{P}(\mathbf{U}|\mathbf{f})\mathcal{P}(\mathbf{f})}{\mathcal{P}(\mathbf{U})} \propto \mathcal{P}_{\mathcal{N}}(\mathbf{U}|G(\mathbf{f})(\mathbf{X}), \beta^{-1}\mathbf{I})\mathcal{P}_{\mathcal{N}}(\mathbf{p}|0, \mathbf{K}_p)\mathcal{P}_{\mathcal{N}}(\mathbf{p}_y|0, \mathbf{K}_p)\mathcal{P}_{\mathcal{N}}(\mathbf{q}|0, \mathbf{K}_q)$$

and the log-likelihood is

$$\mathcal{P}(\mathbf{U}|\mathbf{f}) = -\frac{1}{2}\beta\|\mathbf{U} - G(\mathbf{f})\|^2.$$

To sample from our GP efficiently over the grid \mathbf{t} , we use Cholesky factorization. Indeed, if $w(t) \sim \mathcal{GP}(m, k)$ then $w(\mathbf{t}) \sim \mathcal{N}(\mathbf{m}, \mathbf{k})$, and if $\mathbf{k} = LL^T$ is the Cholesky factorization of \mathbf{k} then we can sample $f(\mathbf{t}) = \mathbf{m} + L\mathbf{s} \sim \mathcal{N}(\mathbf{m}, \mathbf{k})$ by simply sampling $\mathbf{s} \sim \mathcal{N}(0, I)$. The factorization of \mathbf{k} need only be performed once. We use the pre-conditioned Crank-Nicholson scheme (pCN-MCMC) to select the next sample in the chain, as described in Algorithm 1. The pCN-MCMC is similar to, but more efficient than Metropolis-Hastings. The main differences of pCN-MCMC relative to Metropolis-Hastings are that the proposal distribution is identical to the prior distribution Π , the proposal function is a mixture of the previous step in the chain and the new sample, and the acceptance probability is computed using only the log-likelihood instead of the log-joint density. In situations where computation of

Algorithm 1 The pre-conditioned Crank-Nicholson scheme.

```

assume  $f \sim \Pi = \mathcal{GP}(m, k)$ 
make a starting guess  $f^{(0)} \sim \Pi$ 
for  $k = 1$  to  $K$  do
  draw a sample from  $\psi \sim \Pi$ 
   $f^* \leftarrow \sqrt{1 - 2\delta}f^{(k-1)} + \sqrt{2\delta}\psi$  ▷ define new proposal
   $A_k \leftarrow \min\{1, \exp(L(f^*) - L(f^{(k-1)}))\}$  ▷ compute acceptance probability
▷  $L(f)$  is the log-likelihood

  draw  $u_k \sim \mathcal{U}(0, 1)$ 
  if  $u_k < A_k$  then
     $f^{(k)} \leftarrow f^*$  ▷ accept new proposal
  else
     $f^{(k)} \leftarrow f^{(k-1)}$  ▷ reject new proposal
  end if
end for

```

the forward map is more expensive than the case we consider here, a number of methods have been suggested such as using local approximations of the forward map [6], using neural networks [1] or exploiting geometric properties of the posterior [4].

3.1. Assessing convergence. We here discuss methods to assess the convergence of the MCMC algorithm to a stationary distribution. Inference from samples generally suffer from two main issues [9]. The first is insufficient simulation length resulting in samples that do not accurately reflect the underlying distribution. The second is correlations between the samples which reduces the effective number of samples. The first issue can be monitored by having multiple initial guesses and

confirm that they converge to the same distribution. The second issue can be monitored by calculating an effective sample size for the chain to obtain the equivalent number of i.i.d samples. In practice, an effective sample size of 100 is often enough to obtain accurate posterior estimates [9].

3.2. Exploiting prior knowledge through conditioning. One key strength of the Bayesian approach we consider here, is the ability to condition the priors given prior knowledge of the system behavior. The most common case is when the latent functions have known values at a number of points. If a function evaluated at the grid τ has the distribution $f(\tau) \sim \mathcal{N}(\mathbf{m}, \mathbf{K})$ then the conditional distribution on the set of points $(\tau_c, f(\tau_c))$ is

$$f(\tau)|\tau_c, f(\tau_c) \sim \mathcal{N}(\mathbf{m} + \mathbf{k}(\mathbf{K}_c + \sigma^2\mathbf{I})^{-1}(f(\tau_c) - \mathbf{m}_c), \mathbf{K} - \mathbf{k}(\mathbf{K}_c + \sigma^2\mathbf{I})^{-1}\mathbf{k}^T),$$

where \mathbf{K}_c is the covariance function evaluated on τ_c, τ_c , \mathbf{K} is the covariance function evaluated on τ, τ and \mathbf{m}_c is the mean function evaluated at τ_c .

In many cases we cannot condition on specific function values, but instead have a constraint expressed through a linear functional, i.e. $L[f] = l$. An example that we consider later is when the trajectory is known to be closed, i.e. $L[p] = p(T_0) - p(0) = 0$. If $f \sim GP(m, k)$ then the distribution of f conditioned on $L[f] = l$ is $f \sim GP(m_{f|l}, k_{f|l})$ where

$$(32) \quad m_{f|l}(t) = m(t) + \frac{L[k(\cdot, t)]}{L^2[k]}(l - L[m])$$

$$(33) \quad k_{f|l}(t, t') = k(t, t') - \frac{L[k(\cdot, t')]L[k(t, \cdot)]}{L^2[k]},$$

where $L^2[k]$ denotes the application of L to both arguments of k . The ability to flexibly incorporate prior knowledge in a non-parametric way through conditioning is a key advantage of this method.

3.3. Evaluating the forward map efficiently. Since the numerical procedure relies on iteratively computing the forward operator in Eq. (3), we need to perform this computation efficiently. Instead of solving the equation $t = \tau + \|x - p(\tau)\|/c$ for the emission time τ for every measurement point X_i , we consider the set of emission times $\{\tau_i\}_{i=1}^{N_\tau}$ on which we sample the latent functions. We then calculate the corresponding observation times $t = \tau + \|x - p(\tau)\|/c$ for each sensor position. These observation times differ from the measurement times $\{t_i\}_{i=1}^{N_t}$ and we use simple linear interpolation to obtain the forward solution at the given measurement times.

4. NUMERICAL RESULTS

We used two different measurement setups, illustrated in Figure 1, to produce the numerical results shown in this section: one with 424 sensors (field sampling points) distributed approximately uniformly over the hemisphere $\{(x, y, z) \in \mathbf{R}^3, z > 0, x^2 + y^2 + z^2 = 3^2\}$, and one with 213 sensors distributed approximately uniformly over the quarter-sphere $\{(x, y, z) \in \mathbf{R}^3, z > 0, y > 0, x^2 + y^2 + z^2 = 3^2\}$. For visualisation purposes we here confine all source trajectories to the xy -plane.

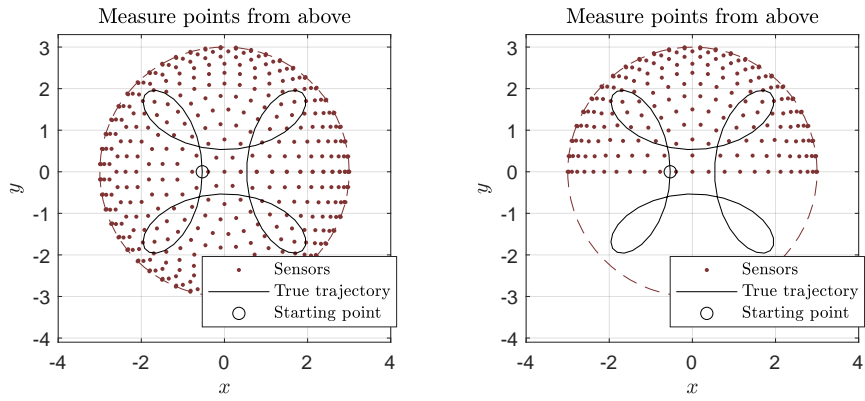


FIGURE 1. Sensor distribution in the two setups (top view).

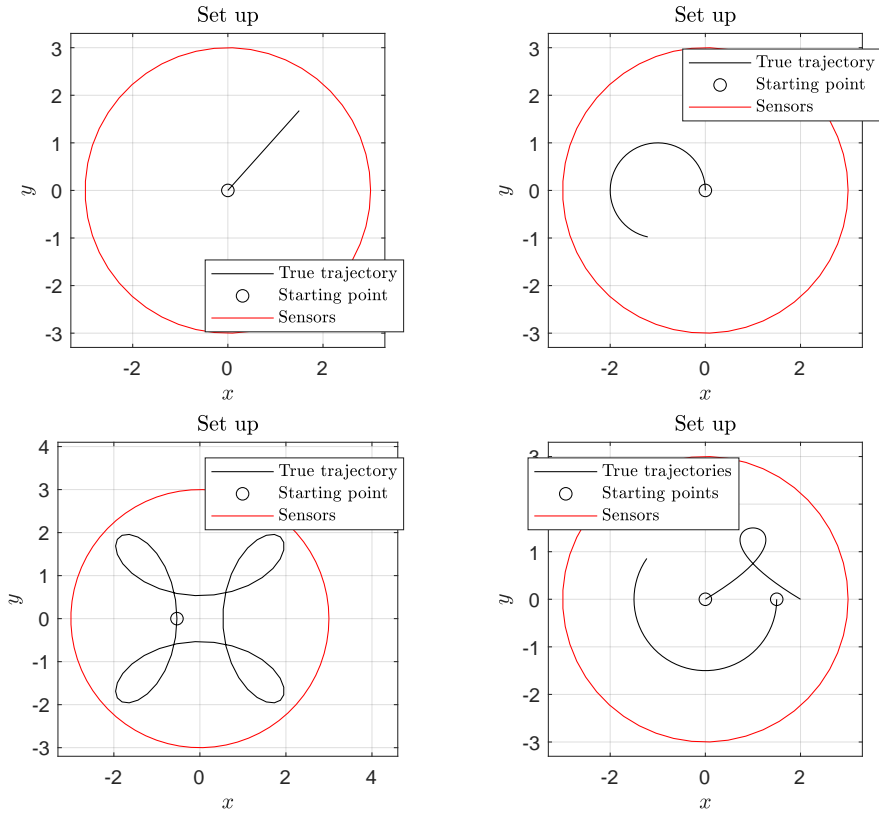


FIGURE 2. Four different trajectories for reconstruction.

Consequently, identical data would be measured at the upper and lower hemispheres. For the target sources, we chose the four trajectories shown in Figure 2, one of which includes two distinct point sources. As intensity profiles we use the

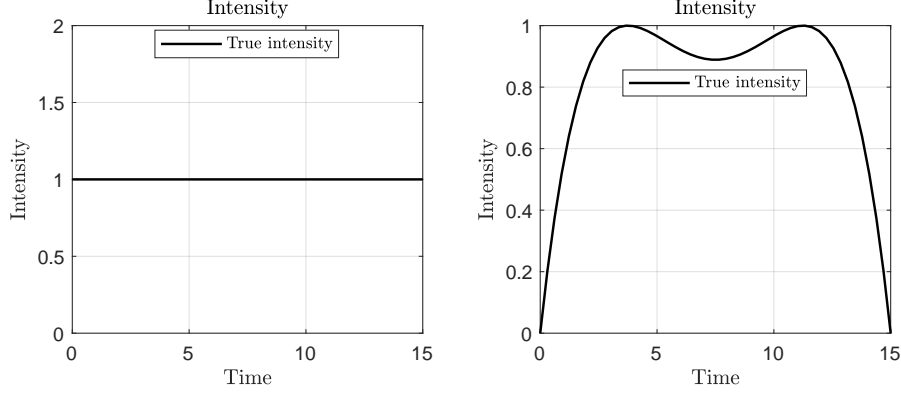


FIGURE 3. Two different intensities for reconstruction.

two intensities shown in Figure 3. All reconstructions used 6 chains of 100.000 samples from the posterior distribution generated by pCN-MCMC, each with a different initial guess of the trajectory and the intensity. The likelihood precision was set to $\beta = 100$, and the pCN parameter to $\delta \in [0.001, 0.0025]$, giving an acceptance ratio close to 25%. The first 50.000 samples in each chain were discarded when calculating the posterior mean. The measuring time was $t \in [0, T] = [0, 20]$, with the source emitting during the interval $t \in [0, T_0] = [0, 15]$. For the 'long trajectory' (the closed curve in Figure 2) $t \in [0, T] = [0, 40]$ and the source emitted during $t \in [0, T_0] = [0, 35]$.

We quantify the errors in the numerical reconstructions $\hat{p}(t)$ and $\hat{q}(t)$ of the posterior trajectory and intensity, respectively, as follows:

$$(34a) \quad \text{trajectory error} = \sqrt{\frac{1}{T_0} \int_0^{T_0} \|\hat{p}(t) - p(t)\|^2 dt}$$

$$\approx \sqrt{\frac{1}{N_t} \sum_{n=1}^{N_t} \|\hat{p}_n - p_n\|^2},$$

$$(34b) \quad \text{intensity error} = \sqrt{\frac{1}{T_0} \int_0^{T_0} (\hat{q}(t) - q(t))^2 dt}$$

$$\approx \sqrt{\frac{1}{N_t} \sum_{n=1}^{N_t} (\hat{q}_n - q_n)^2}.$$

4.1. **Case 1.** Straight-line trajectory in the xy -plane, $p(t) = (v_x t, v_y t, 0)$, $t \in [0, T_0]$, with constant speed $v = \sqrt{v_x^2 + v_y^2} = 0.15$; constant intensity during the emission time,

$$q(t) = \begin{cases} 1, & t \in [0, T_0], \\ 0 & \text{otherwise.} \end{cases}$$

The trajectory and intensity were to be estimated using 424 sensors uniformly distributed on a hemisphere. The measurements of the wave field are shown in Figure 4. As part of our study of Case 1, we investigated the effect of the hyper-

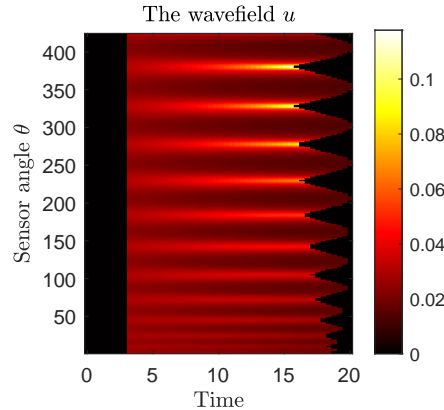


FIGURE 4. The measured wave field in Case 1.

parameter ℓ in the covariance function on the numerical results. Figure 5 shows the initial guesses for the source trajectory corresponding to three different values of ℓ and, as expected, larger values resulted in slower-turning trajectories. Figure 6 shows, for each of the three sets of hyperparameter values, the first 400 samples following one of the initial guesses. Clearly only the best-adapted choice, with the relatively large correlation length, results in apparent convergence towards the true source trajectory. As shown in Figure 7, the subsequent sampling improves the situation for the two other choices of hyperparameter values, but the best-adapted choice still seems to show better convergence to the true source trajectory. Figures 8, 9, 10, and 11 show the modes (the trajectories with the highest posterior density) and means of the posterior trajectories and intensities from the six initial guesses. In all three cases, the posterior means seem to be better predictors than

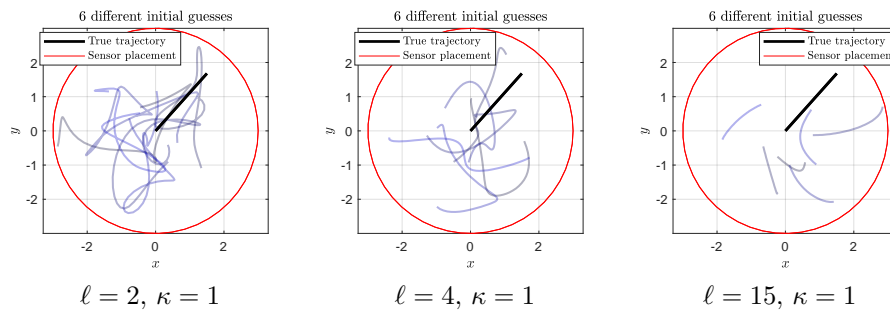


FIGURE 5. Three types of initial guesses.

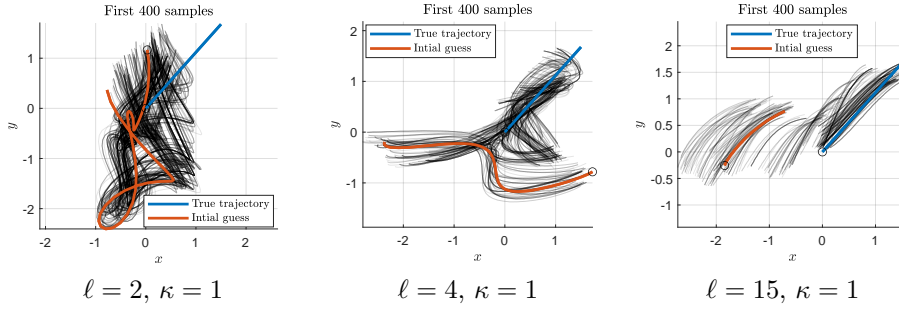


FIGURE 6. First 400 samples from one initial guess.

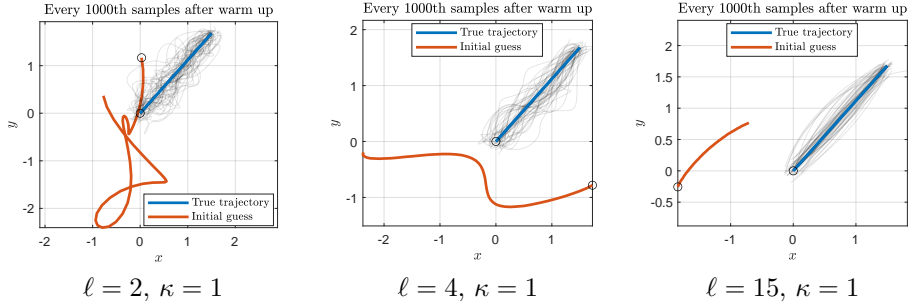


FIGURE 7. Every 1000th sample after warm-up from one initial guess.

the posterior modes. In particular, the posterior means give a significant improvement over the modes when suboptimal hyperparameters are chosen. Table 1 shows the reconstruction errors, defined in Eqs. (34) for the three sets of values of the hyperparameters.

	$\ell = 2, \kappa = 1$	$\ell = 4, \kappa = 1$	$\ell = 15, \kappa = 1$
wavefield error	$9.5 \cdot 10^{-4}$	$7.8 \cdot 10^{-4}$	$6.0 \cdot 10^{-4}$
Average trajectory error	$5.1 \cdot 10^{-2}$	$4.5 \cdot 10^{-2}$	$4.1 \cdot 10^{-2}$
Average intensity error	$3.0 \cdot 10^{-2}$	$1.9 \cdot 10^{-2}$	$1.2 \cdot 10^{-2}$

TABLE 1. Field, trajectory and intensity error for the average (over 6 starting guesses) posterior means for three sets of hyperparameter values.

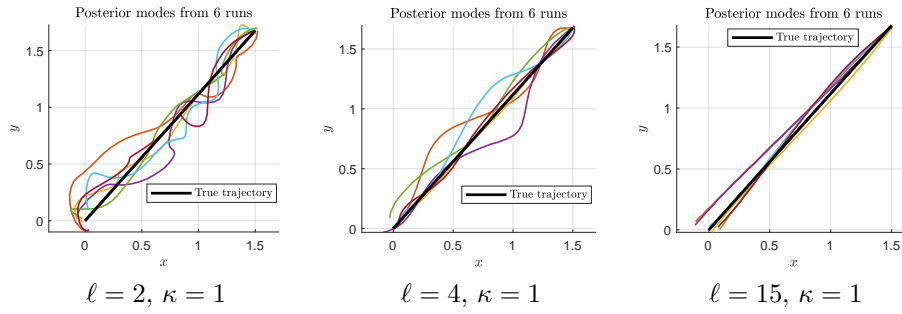


FIGURE 8. Posterior modes of the trajectory from six different initial guesses.

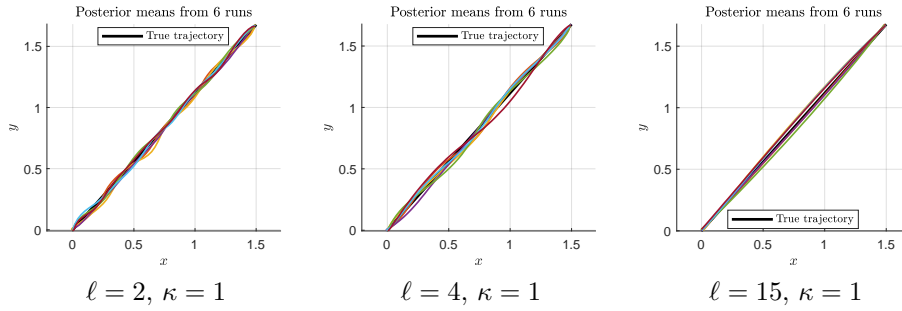


FIGURE 9. Posterior means of the trajectory from six different initial guesses.

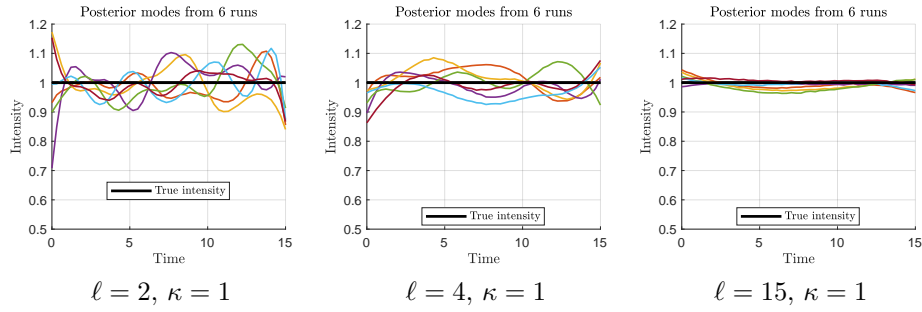


FIGURE 10. Posterior modes of the intensity from six different initial guesses.

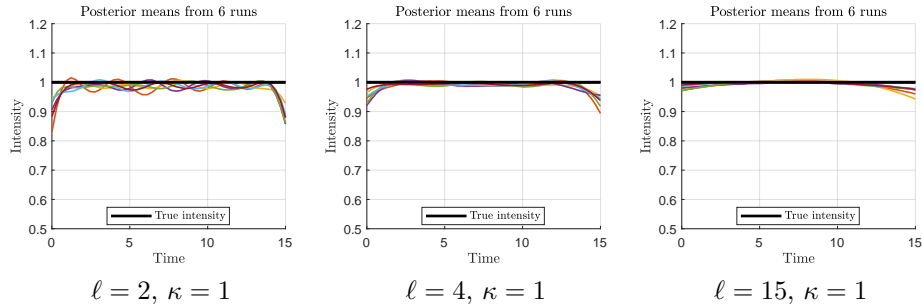


FIGURE 11. Posterior means of the intensity from six different initial guesses.

4.2. **Case 2.** We consider a circular arc trajectory in the xy -plane parametrized by

$$(35) \quad p(t) = (\cos(0.3t) - 1, \sin(0.3t), 0), t \in [0, T_0]$$

and with non-constant polynomial intensity

$$(36) \quad q(t) = \begin{cases} -28.44(t/T_0)^4 + 56.89(t/T_0)^3 - 39.11(t/T_0)^2 + 10.67(t/T_0), & t \in [0, T_0] \\ 0, & \text{otherwise} \end{cases}$$

We use the hyperparameter values $\kappa = 1$, $\ell = 5$ with 6 resulting samples from the GP prior shown in Fig. 12. Figure 13 shows every 1000th sample from six independent MCMC chains together with the corresponding posterior means.

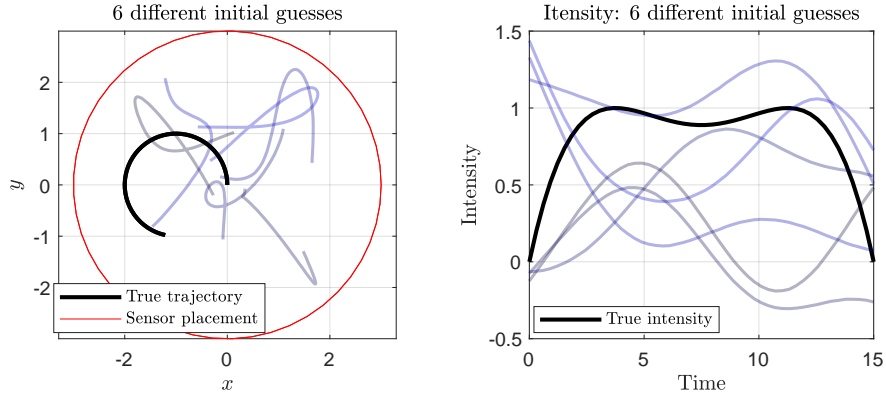


FIGURE 12. Initial samples from the GP prior for the trajectory (left) and intensity (right).

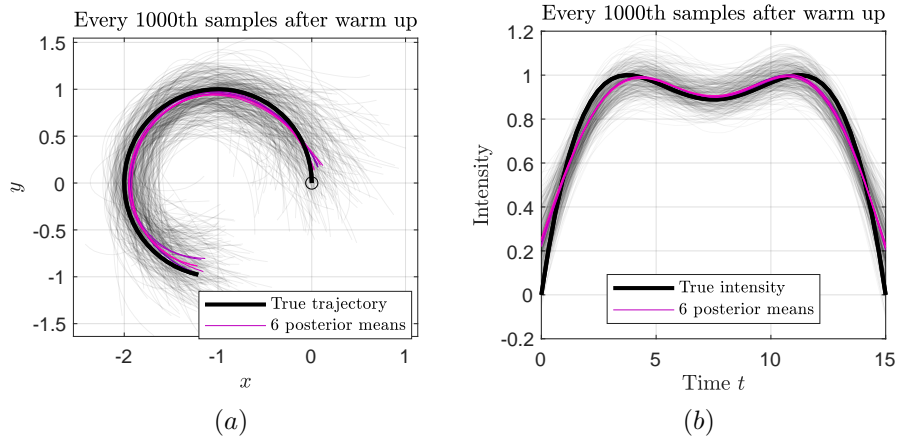


FIGURE 13. Every 1000th sample after warm of from all 6 chains, and their corresponding posterior mean for (a) the trajectory and (b) the intensity.

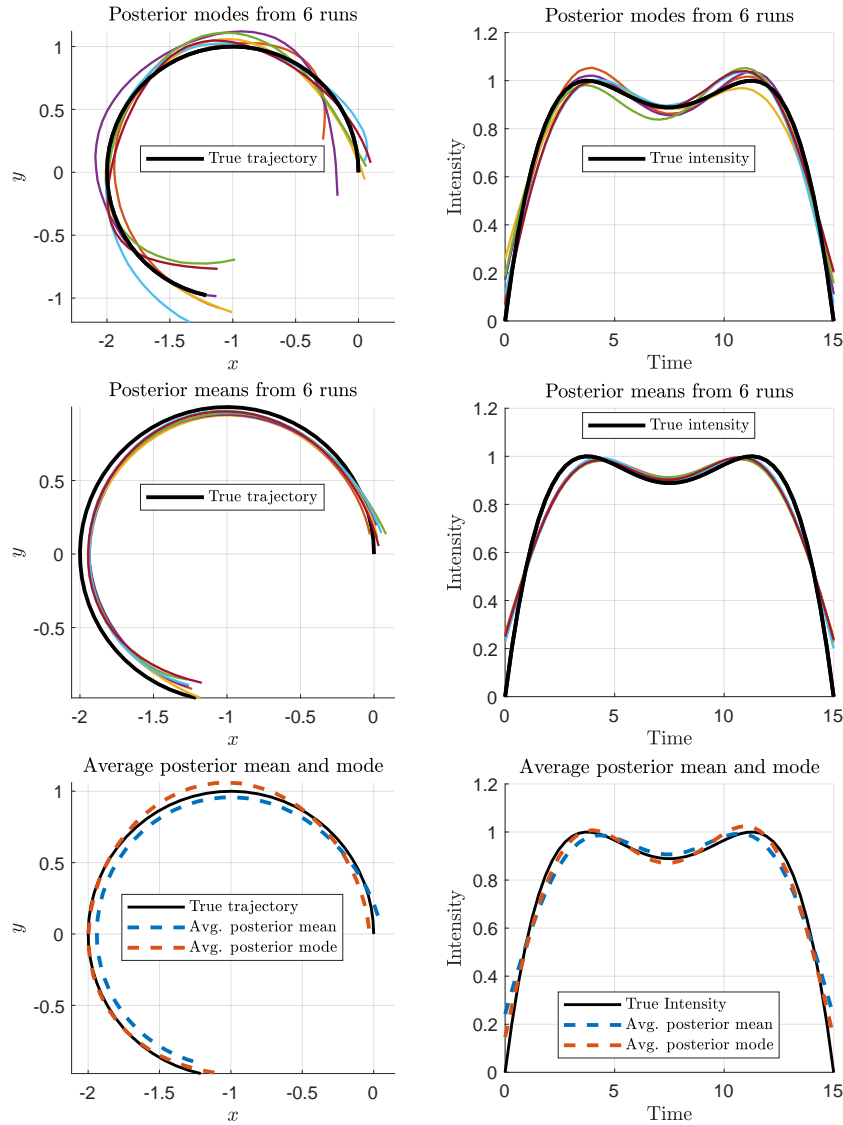


FIGURE 14. Reconstruction with polynomial intensity.

A comparison between the posterior mean, posterior mode and averaged mean and mode over the six chains are shown in Fig. 14. The effective sample size of $N_{\text{eff}} = 656$ is sufficient to represent the posterior distribution. We again see larger variance in the posterior modes than the more conservative posterior means and a slight bias towards origin for the means, possibly due to a slight asymmetry in the posterior distribution. The averaged means and modes give the best reconstruction as quantified in Tbl. 2. We note that the reconstruction is worst near the trajectory end points due to the low emission intensity. We now consider the effect of noisy

	Average mean	Average mode
wavefield error	$1.4 \cdot 10^{-3}$	$8.9 \cdot 10^{-4}$
trajectory error	$5.9 \cdot 10^{-2}$	$4.9 \cdot 10^{-2}$
intensity error	$6.5 \cdot 10^{-2}$	$3.9 \cdot 10^{-2}$

TABLE 2. Error for the average posterior mean and the average posterior mode.

measurements on the reconstruction. We incorporate noise similarly to [20] where at each measurement time $t = t_l$ we set $u_{\text{meas}}(x, t_l) = u(x, t_l) + \epsilon_l$ where u is the noise-free solution with additive time-dependent noise $\epsilon \sim \mathcal{N}(0, \sigma_l^2)$. The noise magnitude is defined relative to the field

$$(37) \quad \sigma_l = \alpha \sqrt{\int_{\Gamma} |u(x, t_l)|^2 dS} \approx \alpha \sqrt{\frac{A(\Gamma)}{N_{\text{sensors}}} \sum_{i=1}^{N_{\text{sensors}}} |u(x_i, t_l)|^2},$$

where $A(\Gamma)$ is the area of the measurement surface. Note that this type of noise is purely time-dependent and is the same across the sensors, which is a harder problem than the case where the noise is also random between the sensors. The resulting reconstructions for $\alpha \in (0, 0.05, 0.25, 0.5)$ are shown in Fig. 15. We obtain a reasonable reconstruction up to 25 % noise with the intensity reconstruction being more affected than the trajectory. Our method seems to be highly resistant to noise due to using whole-trajectory samples compared to algebraic methods where the trajectory is reconstructed pointwise [20]. However, direct comparison is difficult since [20] considers three simultaneous sources for reconstruction.

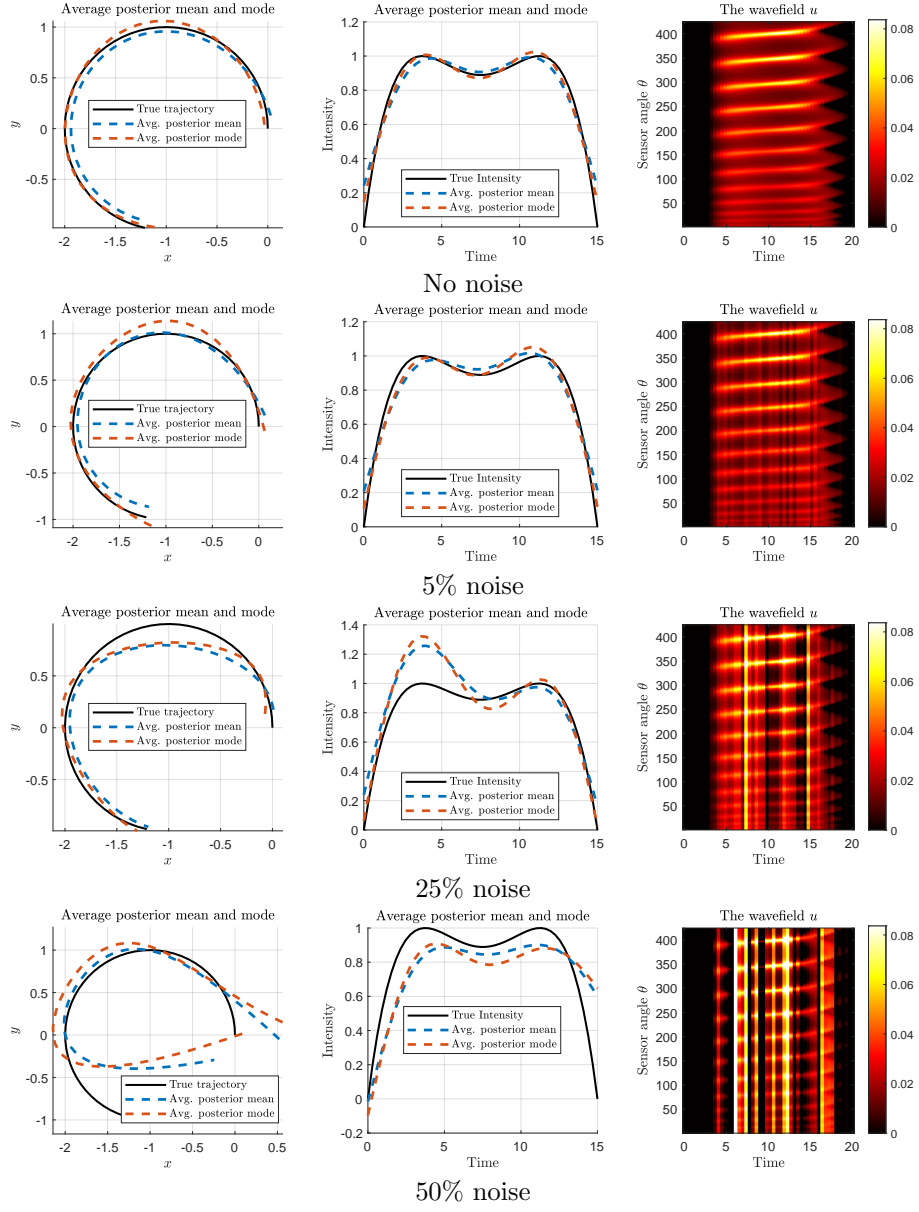


FIGURE 15. Reconstruction with polynomial intensity with no noise, 5%, 25% and 50% noise.

4.3. **Case 3.** We now consider a more complicated and longer trajectory with multiple crossing points given in parametric form as

$$p_x(t) = \frac{8}{5} \sin(2\pi t/T_0 + 3\pi/2) + \frac{16}{15} \cos(6\pi t/T_0), \quad t \in [0, T_0],$$

$$p_y(t) = \frac{8}{5} \cos(2\pi t/T_0 + 3\pi/2) + \frac{16}{15} \sin(6\pi t/T_0), \quad t \in [0, T_0],$$

$$p_z(t) = 0, \quad t \in [0, T]$$

with the same emission intensity considered earlier

(38)

$$q(t) = \begin{cases} -28.44(t/T_0)^4 + 56.89(t/T_0)^3 - 39.11(t/T_0)^2 + 10.67(t/T_0), & t \in [0, T_0] \\ 0, & \text{otherwise} \end{cases}$$

We fix the hyperparameters $\kappa = 1.2$, $\ell = 4$. The trajectory and intensity with a number of initial draws from the GP prior are shown in Fig. 16. Figure 17

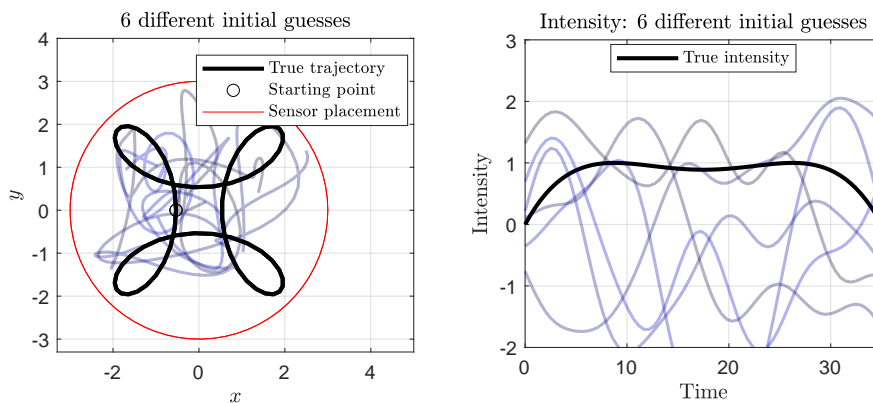


FIGURE 16. The setup for the long trajectory. The source initially travels in the positive y -direction.

shows every 1000th sample from the pCN-MCMC chain together with the posterior means. We obtain a good reconstruction of the intensity while the trajectory deviates near the trajectory endpoints due to the low intensity near $t = 0$ and $t = T_0$. A comparison of the posterior mean and mode averaged over 6 chains is shown in Fig. 18 and we see that while the averaged mode is slightly better than the averaged mean, the endpoint problem persists. This is reflected in the average trajectory error in Tbl. 3 compared to the previous cases. We now show how

	Average mean	Average Mode
wavefield error	$2.0 \cdot 10^{-3}$	$1.7 \cdot 10^{-3}$
Average trajectory error	$2.3 \cdot 10^{-1}$	$2.2 \cdot 10^{-1}$
Average intensity error	$1.7 \cdot 10^{-2}$	$2.0 \cdot 10^{-2}$

TABLE 3. Error of the average posterior mean and mode.

the reconstruction can be greatly aided by incorporating the prior knowledge that the trajectory is closed as discussed in Sec. 3.2. Note that we use no knowledge of the exact trajectory coordinates at any time, we only condition the prior on $p(0) = p(T_0)$. This leads to the reconstruction in Fig. 20. Visually, the reconstruc-

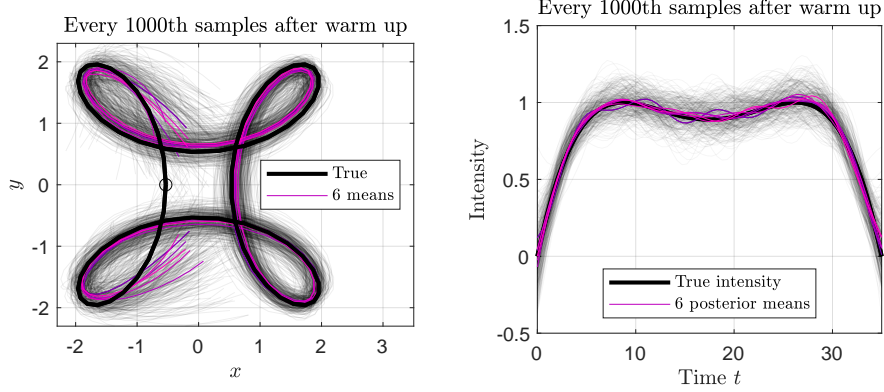


FIGURE 17. Every 1000th sample from all 6 chains and their corresponding posterior mean.

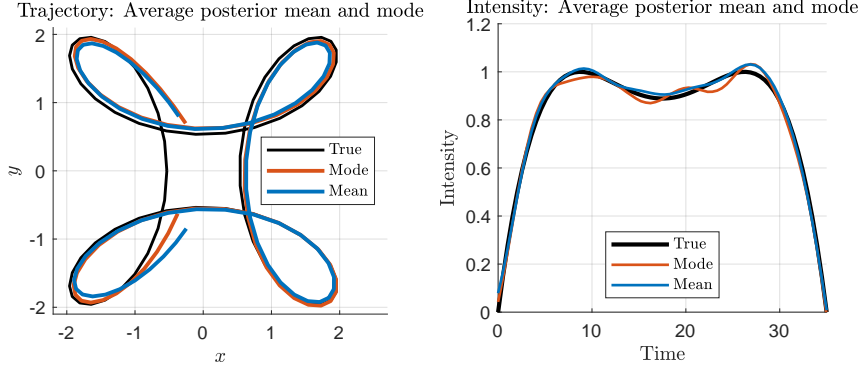


FIGURE 18. The average posterior mean and mode of the trajectory and intensity.

tion of the trajectory has significantly improved: The prior provides information where the reconstruction previously suffered due to the low intensity. We still see some deviation near the endpoints and reconstruction could be further improved by conditioning on a smooth joining of the endpoint, i.e. $p'(0) = p'(T_0)$. Tbl. 4 shows how the trajectory reconstruction has improved through the simple single-point conditioning. The ability to incorporate prior information in such a flexible way is a key advantage of this method compared to e.g. algebraic methods which rely on point-wise estimation. Lastly, we show how the choice of measurement sur-

	Not conditioned	Conditioned
wavefield error	$2.0 \cdot 10^{-3}$	$1.7 \cdot 10^{-3}$
Average trajectory error	$23 \cdot 10^{-2}$	$11 \cdot 10^{-2}$
Average intensity error	$1.7 \cdot 10^{-2}$	$2.5 \cdot 10^{-2}$

TABLE 4. Errors using the average posterior mean from conditioned and unconditioned model.

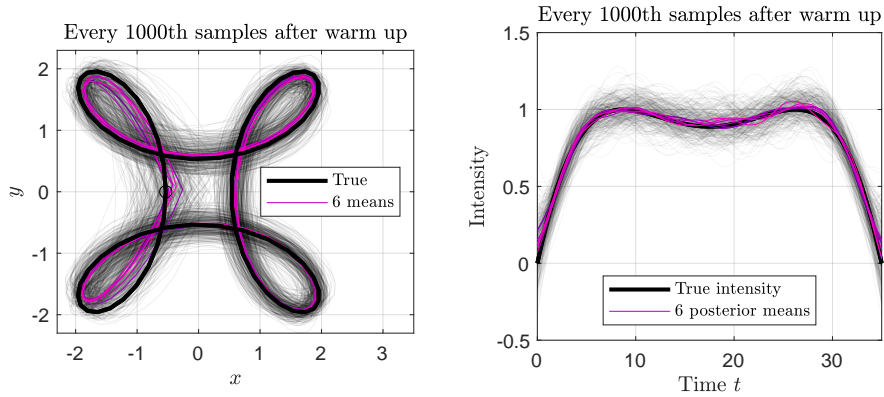


FIGURE 19. Every 1000th sample from 6 chains and the corresponding posterior means with closed-curve conditioning.

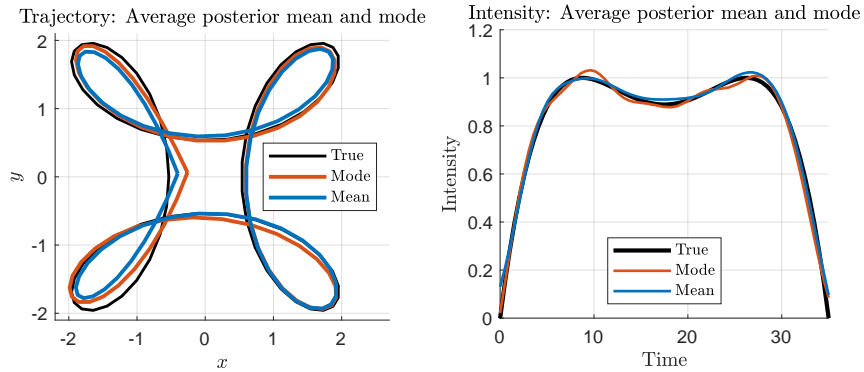


FIGURE 20. The average posterior mean and mode of the trajectory and intensity with closed-curve conditioning.

face influences the reconstruction. We again condition on a closed trajectory but remove half the measurement points, leaving 213 sensors in a quarter sphere. The resulting reconstruction is shown in Fig. 22. The impact on the reconstruction is evident: The reconstruction suffers significantly in the lower half while we retain a good reconstruction in the upper half. A similar effect is observed in the intensity reconstruction, where the time interval $[10, 20]$ corresponds to the particle travelling in the lower half of the trajectory.

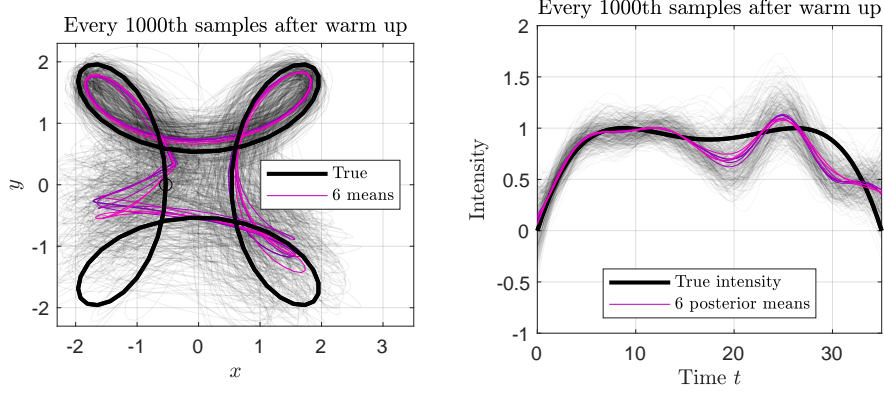


FIGURE 21. Every 1000th sample from all 6 chains, and their posterior mean.

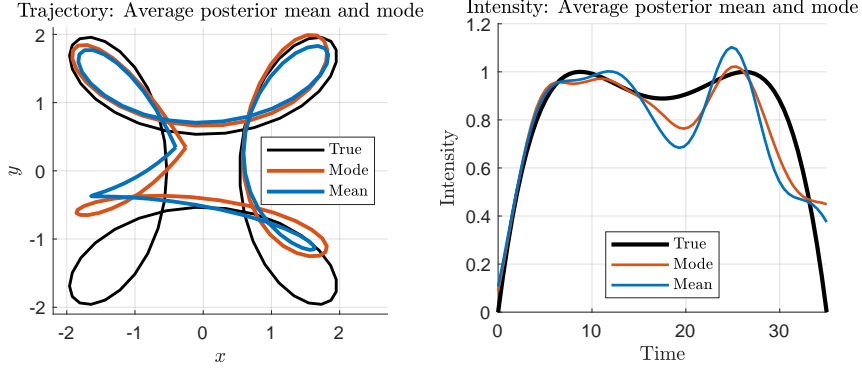


FIGURE 22. The average posterior mean and mode of the trajectory and intensity.

4.4. **Case 4.** As a final example we demonstrate how our method performs in the presence of two simultaneously radiating sources. We consider the trajectories given in parametric form by

$$(39a) \quad p_1(t) = (16(t/T_0)^3 - 24(t/T_0)^2 + 5t/T_0, 3(t/T_0)(1 - t/T_0), 0), \quad t \in [0, T_0]$$

$$(39b) \quad p_2(t) = (1.5 \cos(0.25t), -1.5 \sin(0.25t), 0), \quad t \in [0, T_0]$$

with constant emission intensity

$$q_1(t) = q_2(t) = 1, \quad t \in [0, T_0], \quad q_1(t) = q_2(t) = 0, \quad t > T_0$$

and we choose the hyperparameters $\kappa = 1$ and $\ell = 5$ for all priors for the reconstruction. Figure 23 shows the trajectories and the distribution of 424 sensors over a hemisphere together with the measured wave field. Figure 24 shows the trajectories and intensities together with two draws from the prior distribution. We then generate 100.000 samples from the MCMC algorithm and the resulting Bayesian reconstruction is shown in Fig. 25, showing the posterior mean and mode

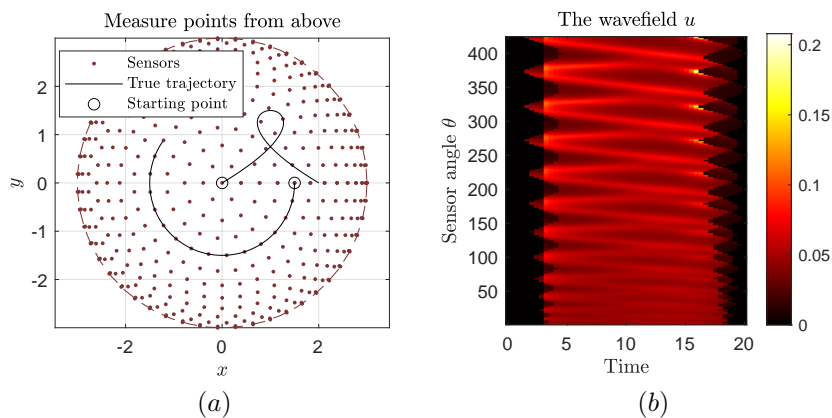


FIGURE 23. The setup: (a) shows the trajectories and sensor placement from above and (b) shows the measurement data.

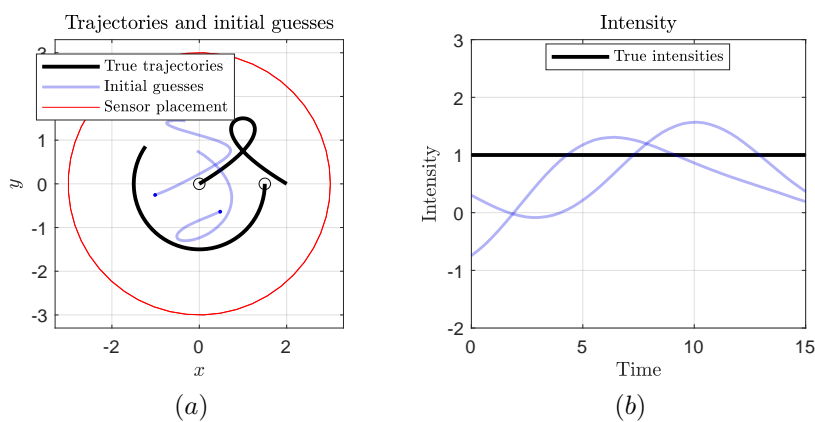


FIGURE 24. Initial guesses of (a) the trajectories and (b) the intensity for two sources.

together with every 500th sample from the MCMC chain. While the reconstruction still yields reasonable results, we see that the reconstruction suffers slightly when another emitter is introduced compared to the single-emitter case.

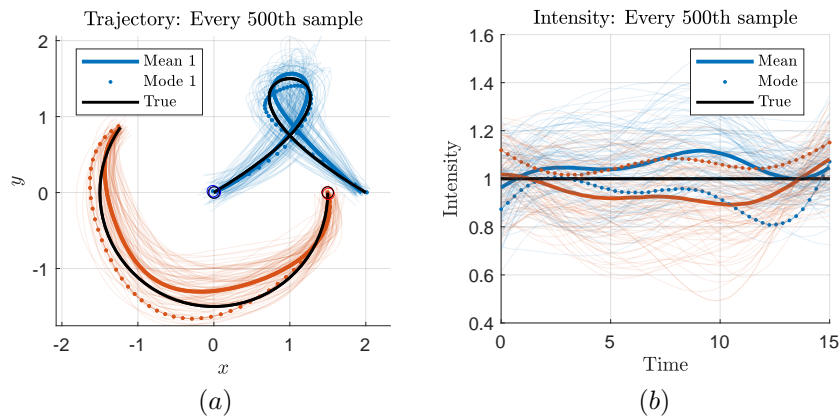


FIGURE 25. Posterior mean, mode and every 500th sample of (a) the trajectories and (b) the intensities. The coloured solid lines are the posterior means and the dotted lines are the posterior modes.

REFERENCES

- [1] Harbir Antil, Howard C Elman, Akwum Onwunta, and Deepanshu Verma. Novel deep neural networks for solving bayesian statistical inverse. *arXiv preprint arXiv:2102.03974*, 2021. [10](#)
- [2] Gang Bao, Yuantong Liu, and Faouzi Triki. Recovering point sources for the inhomogeneous helmholtz equation. *Inverse Problems*, 37(9):095005, 2021. [3](#)
- [3] Gang Bao, Yuantong Liu, and Faouzi Triki. Recovering simultaneously a potential and a point source from cauchy data. *Minimax Theory and its Applications*, 06(2):227–238, 2021. [3](#)
- [4] Alexandros Beskos, Mark Girolami, Shiwei Lan, Patrick E Farrell, and Andrew M Stuart. Geometric mcmc for infinite-dimensional inverse problems. *Journal of Computational Physics*, 335:327–351, 2017. [10](#)
- [5] Gottfried Bruckner and Masahiro Yamamoto. Determination of point wave sources by point-wise observations: stability and reconstruction. *Inverse problems*, 16(3):723, 2000. [3](#)
- [6] Patrick R Conrad, Youssef M Marzouk, Natesh S Pillai, and Aaron Smith. Accelerating asymptotically exact mcmc for computationally intensive models via local approximations. *Journal of the American Statistical Association*, 111(516):1591–1607, 2016. [10](#)
- [7] H. Duistermaat. *Distributions: Theory and Applications*. Birkhäuser, 2010. [5](#)
- [8] Abdellatif El Badia and T Ha-Duong. Determination of point wave sources by boundary measurements. *Inverse Problems*, 17(4):1127, 2001. [3](#)
- [9] Andrew Gelman, John B Carlin, Hal S Stern, and Donald B Rubin. *Bayesian data analysis*. Chapman and Hall/CRC, 2013. [10](#), [11](#)
- [10] A. Elbadia H. Al Jebawy and F. Triki. Inverse moving point source problem for the wave equation. *Arxiv*, 2022. [3](#)
- [11] L. Hörmander. *The Analysis of Linear Partial Differential Operators I*. 2003. [1](#), [2](#), [4](#)
- [12] G. Hu, Y. Kian, P. Li, and Y. Zhao. Inverse moving source problems in electrodynamics. *Inverse Problems*, 35:075001, 2019. [3](#)
- [13] G. Hu, Y. Liu, and M. Yamamoto. Inverse moving source problem for fractional diffusion (-wave) equations: Determination of orbits. In *International Conference on Inverse Problems*, pages 81–100. Springer, 2018. [3](#)
- [14] J. D. Jackson. *Classical electrodynamics*. 1999. [2](#)
- [15] Vilmos Komornik and Masahiro Yamamoto. Upper and lower estimates in determining point sources in a wave equation. *Inverse Problems*, 18(2):319, 2002. [3](#)
- [16] Vilmos Komornik and Masahiro Yamamoto. Estimation of point sources and applications to inverse problems. *Inverse Problems*, 21(6):2051, 2005. [3](#)
- [17] E. Nakaguchi, H. Inui, and K. Ohnaka. An algebraic reconstruction of a moving point source for a scalar wave equation. *Inverse Problems*, 28:065018, 2012. [3](#)

- [18] Etsushi Nakaguchi, Hirokazu Inui, and Kohzaburo Ohnaka. An algebraic reconstruction of a moving point source for a scalar wave equation. *Inverse Problems*, 28(6):065018, 2012. [3](#)
- [19] J.-C. Nédélec. *Acoustic and Electromagnetic Equations: Integral Representations for Harmonic Problems*. Springer, 2001. [6](#)
- [20] T. Ohe. Real-time reconstruction of moving point/dipole wave sources from boundary measurements. *Inverse Problems in Science and Engineering*, 28:1057–1102, 2020. [3](#), [19](#)
- [21] Takashi Ohe, Hirokazu Inui, and Kohzaburo Ohnaka. Real-time reconstruction of time-varying point sources in a three-dimensional scalar wave equation. *Inverse Problems*, 27(11):115011, 2011. [3](#)
- [22] Kamal Rashedi and Mourad Sini. Stable recovery of the time-dependent source term from one measurement for the wave equation. *Inverse Problems*, 31(10):105011, 2015. [3](#)